Ionization of Rydberg atoms at patterned electrode arrays

Y. Pu and F. B. Dunning

Department of Physics and Astronomy and the Rice Quantum Institute, Rice University MS-61, Houston, Texas 77005-1892, USA

Lithographically patterned micrometer-scale electrode arrays are used to examine the effects of controlled surface electric fields on Rydberg-atom–surface interactions. The data show that application of modest electrode biases ($\sim \pm 1$ V) can lead to a transition from ionization of the incident atoms by short-range tunneling to field ionization well above the target surface. The resulting ions can be efficiently detected using ion collection fields whose strengths are substantially smaller than those required for direct field ionization pointing to the application of surface ionization in the detection of low-n Rydberg atoms. The data are analyzed with the aid of a Monte Carlo model and further demonstrate the critical role that local surface fields can play in governing the nature of atom-surface interactions.

PACS number(s): 34.35.+a, 32.80.Ee, 34.70.+e

I. INTRODUCTION

While the surfaces of conductors are often viewed as an equipotential, in reality surface microstructure or the presence of adsorbates can lead to local potential variations and to the appearance, near the surface, of strong surface "patch fields." Strong local fields can also be generated at insulating surfaces through surface charging. The presence of such strong surface fields can dramatically influence atom-surface interactions. For example, patch fields can affect the behavior of ions and atoms trapped near a surface [1–7] and can impact studies of short-range surface phenomena such as the Casimir Polder force [8,9] and noncontact friction [10–12]. Measurements of surface fields are therefore important to assess their likely impact and to explore means to control them.

Because of their large physical size, $\sim n^2$ a.u., Rydberg atoms are strongly perturbed by external electric fields and can provide a powerful probe of local fields. For example, Rydberg atoms display pronounced Stark shifts and measurements of such shifts have been used to map stray fields above an atom chip and fields resulting from alkali-metal deposition [5,12–14]. Patch fields at smaller atom-surface separations have been investigated by studying the ionization of Rydberg atoms incident on the surface at near-grazing incidence in the presence of an ion collection field. Comparisons between theoretical predictions [15–20] and experimental measurements [21–26] have revealed the presence of strong local surface fields. Close to a conducting surface, ionization can occur through resonant tunneling of the excited electron into a vacant level in the surface. Stray fields (and the presence of the ion collection field) modify the potential barrier between the atom and surface and thus the atom-surface separation at which ionization occurs. Once formed, an ion experiences forces from its image charge and the local surface patch field which must be overcome by the ion collection field in order to accelerate the ion away from the surface and detect it. Measurements of the ion signal as a function of the collection field can thus provide a measure of the stray fields present at the surface. Studies of conducting surfaces reveal strong local patch fields that can be as large as $\sim 10^3$ V cm^{-1} even 100 nm from the surface, and point to potential variations across the surface of up to $\sim \pm 75$ mV on length scales of ~ 100–500 nm. Measurements at Si(100) surfaces having

a robust native oxide layer display even larger patch field effects [27].

Variations in surface potential of even a few tenths of a volt, however, are small compared to those that can be achieved by applying potentials to micrometer-scale electrode arrays lithographically patterned on a substrate. Furthermore, such structures provide the opportunity to control and manipulate the strength (and geometry) of the surface field. In the present work we explore the effects of such engineered fields using xenon Rydberg atoms with values of principal quantum number n in the range $18 \leqslant n \leqslant 32$ incident on electrode arrays comprised of a series of parallel electrodes with alternating positive and negative biases. The data, which are analyzed with the aid of Monte Carlo simulations, demonstrate that, even for modest electrode biases ($\sim \pm 1$ V), the resulting surface fields can lead to dramatic changes in the nature of the atom-surface interaction. In particular, for sufficiently large biases, rather than being ionized by tunneling near the surface, incident atoms undergo field ionization well above the surface and a larger fraction of the Rydberg atoms incident on the surface can be detected as ions. The present work further illustrates the important role local surface fields can play in atom-surface interactions and suggests that ionization in controlled surface fields can provide a convenient means to detect low-n Rydberg atoms.

II. EXPERIMENTAL APPARATUS

The present experimental apparatus is shown in Fig. 1 and its operation is described in detail elsewhere [21]. Briefly, thermal-energy xenon Rydberg atoms are directed at near-grazing incidence, $\theta \sim 5°$–$10°$, onto a patterned surface electrode array. As they approach the surface the Rydberg atoms are ionized in the presence of an ion collection field applied perpendicular to the surface. Those ions that escape the surface are accelerated to a bell-mouthed channeltron for detection.

The xenon Rydberg atoms are created by photoexciting the $^3P_0$ atoms contained in a mixed beam of Xe($^3P_0$) and Xe($^3P_2$) metastable atoms that is created by electron impact excitation of ground-state atoms contained in a supersonic expansion. To obtain a well-defined angle of incidence the
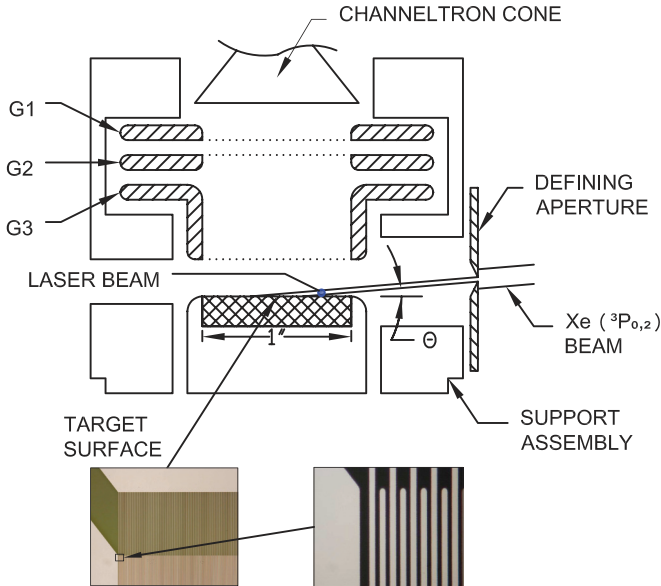
FIG. 1. (Color online) Schematic diagram of the apparatus. The inset shows an optical image of a segment of an array with electrode widths and spacings of 4 μm.

metastable beam is tightly collimated using an 80-μm-wide by 4-mm-high aperture located ~3 cm upstream from the target surface. Xe(nf) Rydberg atoms are created close to the target surface using the focused output of an extracavity-doubled frequency-stabilized Ti:sapphire laser. The laser is polarized perpendicular to the surface to excite $m = 0$ states. Experiments are conducted in a pulsed mode. The output of the laser is formed into a train of pulses of ~1 μs duration and ~3 kHz repetition frequency using an acousto-optic (A-O) modulator. Excitation occurs in (near) zero electric field, i.e., with no ion collection field present and with no biases applied to the electrode array. Immediately following excitation the ion collection field, which has a rise time of ~1 μs and a duration of ~25 μs, is applied. [As this field increases the initial Xe(nf) states correlate with the lowest members of their neighboring Stark manifolds.] At the same time the electrode array is biased to establish the desired surface electric field. Because the flight time of a metastable atom from its point of formation to the target surface is typically ~6–10 μs, arrival time gating is employed to identify those ions produced through atom-surface interactions. The mechanisms responsible for ionization are inferred from measurements of the surface ionization signal as a function of applied ion collection field. To obtain the absolute efficiency with which Rydberg atoms incident on the surface are detected as ions, the number of Rydberg atoms initially created is measured by field ionization induced by a large pulsed electric field applied immediately after the laser pulse. This number is then corrected for radiative decay of the Rydberg atoms during their transit to the surface.

The relatively large surface area illuminated by the incident metastable atoms, and hence the Rydberg atoms, requires the use of an electrode array with dimensions of ~5 × 5 mm². Arrays comprising two interleaved "comblike" structures were employed. Attempts to fabricate arrays with widths and spacings of ~1 μm using electron beam lithography failed because the resulting electrodes were not conducting on length scales greater than ~100 μm. It was therefore decided to use wider electrodes patterned (by a commercial vendor [28]) using direct print technology on a highly reflective photomask blank comprising a 90-nm-thick chromium film deposited on a glass substrate. Test samples showed that over 98% of "wires" with lengths ~5 mm and widths >4 μm fabricated using this technology had good electrical conductivity, and that interelectrode spacings >4 μm were sufficient to ensure that no spurious interelectrode connections remained. Electrode arrays with widths and separations greater than 4 μm are therefore employed in the present work. Optical images of a segment of a typical electrode array are shown in the inset in Fig. 1 and reveal a well-defined pattern of parallel electrodes. The two interleaved sets of electrodes are biased with equal but opposite voltages, $\pm V_B$. The surfaces of the electrode arrays were cleaned prior to insertion in the vacuum chamber by ultrasonic cleaning in a heated (~65 °C) bath of dimethyl sulfoxide.

III. SIMULATIONS

The experimental data are analyzed with the aid of Monte Carlo simulations. The first step in these simulations is the determination of the electric field produced above the surface by the biased electrodes. This is accomplished by solving Laplace's equation using the (known) boundary conditions set by the potentials applied to the electrodes. In defining the boundary conditions it is assumed that the surface is flat, i.e., the 90-nm difference in height between the surface of the electrodes and the substrate surface (which is very much less than the electrode spacing and the atom-surface separation at which ionization typically occurs) is ignored. Since in the present work the emphasis is on the surface field generated by the electrode array, we only consider here electrode biases $V_B \geqslant \pm 0.5$ V that are significantly larger than the local variations in surface potential typically associated with surface inhomogeneities. Under these conditions the local fields that the electrodes generate dominate the atom-surface interaction. This permits stray patch fields to be ignored and allows the surfaces of the electrodes to be treated as equipotentials. The potential of the substrate surfaces is assumed to vary linearly across the gap between neighboring electrodes.

Consider a coordinate system in which the xy plane defines the surface and the z axis is directed perpendicular to the surface in the direction of the outward normal. Assuming that the electrodes lie parallel to the y axis and are very long compared to their width, there will be no y dependence in the surface potential. The electric fields generated by the electrodes therefore have no y component and lie in an xz plane. For the present geometry Laplace's equation reduces to

$$\frac{\partial^2 \phi}{\partial x^2} + \frac{\partial^2 \phi}{\partial z^2} = 0, \qquad (1)$$

where ϕ is the potential. This is satisfied by linear combinations of periodic functions of the form

$$\phi(x,z) = \sum_{i=1}^{\infty} (A_i \cos k_i x + B_i \sin k_i x) e^{-k_i z}, \qquad (2)$$

where $k_i = 2\pi i/D$ and D is the period of the surface potential which is twice that of the electrodes themselves. Using this expression the potential at the surface can be written as

$$\phi(x,0) = \sum_{i=1}^{\infty} (A_i \cos k_i\, x + B_i \sin k_i\, x), \qquad (3)$$

which is simply the Fourier expansion of the surface potential as defined by the electrode biases. The surface potential is therefore represented using a Fourier series yielding the coefficients

$$A_i = \frac{2}{D}\int_0^D \phi(x,0)\cos k_i x\, dx,$$
$$\qquad (4)$$
$$B_i = \frac{2}{D}\int_0^D \phi(x,0)\sin k_i x\, dx.$$

If the origin of coordinates is taken to be at the center of an electrode, the surface potential becomes an even function of x and the potential at any point above the surface can be written as

$$\phi(x,z) = \sum_{i=1}^{N} A_i \cos(k_i x) e^{-k_i z}. \qquad (5)$$

In practice, the Fourier components included in Eq. (5) were limited to those with wavelengths D/i greater than 250 nm. (Tests showed that neglect of the shorter wavelength components produced no significant changes in the predicted surface ionization characteristics, not surprising since their

contributions to the surface field decrease rapidly with z.) The magnitude of the electric field above the electrode array is derived by taking the gradient of the potential and is given by

$$|E(x,z)| = \left[\left(-\frac{\partial\varphi}{\partial x}\right)^2 + \left(-\frac{\partial\varphi}{\partial z}\right)^2\right]^{1/2}$$

$$= \frac{2\pi}{D}\left[\left(\sum_{i=1}^{N} A_i i\, \sin\frac{2\pi i}{D}x\, e^{-\frac{2\pi i}{D}z}\right)^2\right.$$

$$\left. + \left(\sum_{i=1}^{N} A_i i\, \cos\frac{2\pi i}{D}x\, e^{-\frac{2\pi i}{D}z}\right)^2\right]^{1/2}. \qquad (6)$$

Interestingly, for arrays of electrodes with equal widths and equal but opposite biases $\pm V_B$, at large values of z the leading ($i = 1$) term becomes dominant and Eq. (6) can be approximated as

$$|E(x,z)| = \frac{2\pi A_1}{D}\left(\sin^2\frac{2\pi}{D}x\, e^{-\frac{4\pi}{D}z} + \cos^2\frac{2\pi}{D}x\, e^{-\frac{4\pi}{D}z}\right)^{1/2}$$

$$= \frac{2\pi A_1}{D}e^{-\frac{2\pi}{D}z}, \qquad (7)$$

i.e., the magnitude of the electric field becomes independent of x.

Typical values of the electric field are presented in Fig. 2 for electrode widths and spacings of 4 and 16 μm and biases representative of those employed in the present study. Even for biases of ± 1 V the fields can be large and extend a sizeable distance from the surface. The peak fields immediately above
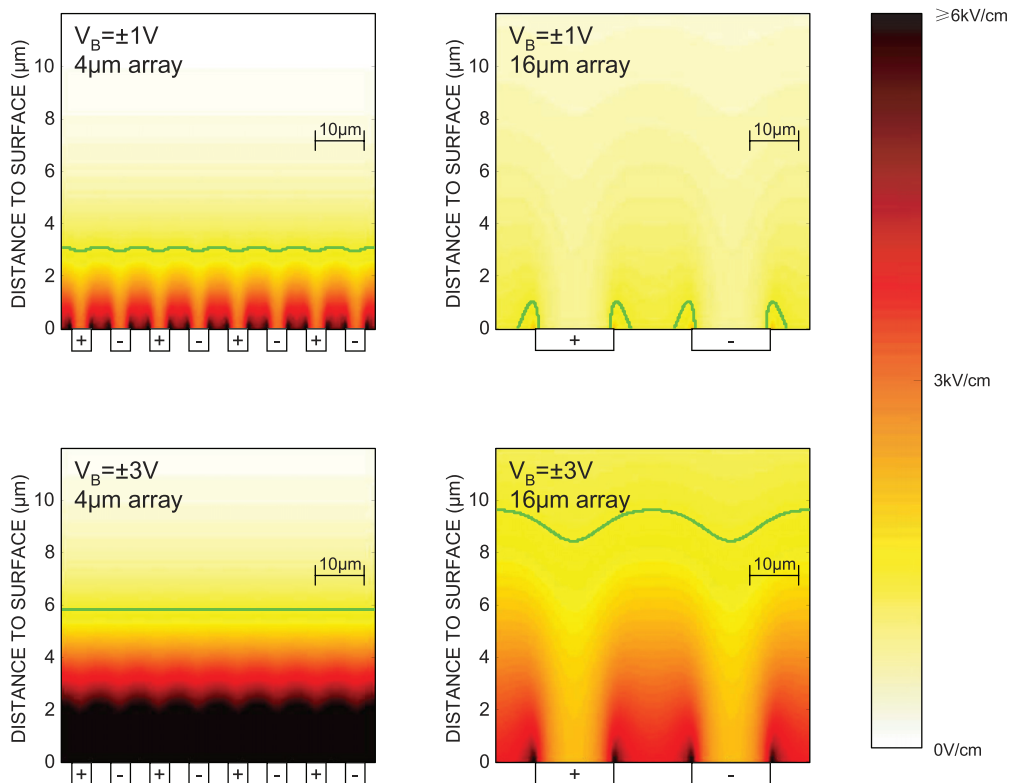

FIG. 2. (Color online) Calculated magnitudes of the electric fields above electrode arrays with the widths and spacings, and the biases, indicated. The lines show the locus of points where the field magnitude is sufficient to ionize $n = 23$ atoms.

the 4-μm electrode array are larger than those above the 16-μm array. However, because of the larger periodicity of the 16-μm array the fields it generates decay less rapidly with distance from the surface. The lines in the figures show the locus of points where the field is sufficient to ionize incident $n = 23$ Rydberg atoms. As will be justified later, in determining the point of ionization it is assumed that the incident atoms evolve adiabatically in the changing electric field that they experience as they approach the surface. Ionization is presumed to occur when the (Stark shifted) energy of the Rydberg electron first dips below the saddle point in the electron potential that results from the presence of the surface (and applied ion collection) fields. Such (adiabatic) ionization occurs at fields of $\sim 1/16n^4$ a.u. In the case of the 4-μm electrode array ionization is predicted to occur relatively far from the surface at atom-surface separations of a few micrometers, much larger than those characteristic of ionization through tunneling into vacant surface levels at a conductor which are given by $\sim (3–4)n^2$ a.u. [13], and amount to ~ 100 nm for atoms with $n = 23$. Ionization also occurs relatively far from the surface of the 16-μm electrode array when sizable biases are applied. For small biases, however, fields sufficiently strong to ionize $n = 23$ atoms are only present at the edges of the electrodes. Nonetheless, as will be discussed below, atoms incident at near-grazing angles tend to ionize near the "peaks" in the ionization profile and many will still ionize relatively far from the surface.

The effect of the applied ion collection field is illustrated in Fig. 3 which shows the magnitude of the combined

FIG. 3. (Color online) Calculated magnitudes of the electric field above electrode arrays with widths and spacings of 8 μm biased at ± 1 V, and the applied ion collection fields F_c indicated. The solid lines show the locus of points where the field magnitude is sufficient to ionize $n = 23$ atoms. The dashed lines indicate trajectories of atoms incident at $\theta = 10°$ and their spacing encompasses one period of the electrode array. Atoms ionized at points indicated by white (black) dots are collected by the ion collection field (lost to the surface).

ion collection and surface fields above an electrode array with widths and spacings of 8 μm biased at ± 1 V for representative values of the applied ion collection field. As expected, application of an ion collection field increases the magnitude of the local fields adjacent to and above the positively biased electrodes. Figure 3 again includes the locus of points at which the field is sufficient to ionize incident $n = 23$ atoms. As the ion collection field is increased this locus of points becomes increasingly peaked near the positive electrodes, the peaks moving progressively further from the surface.

Following ionization, the trajectories of the product ions in the combined surface and ion collection fields are computed using a Runge-Kutta algorithm. If the ion is directed towards the surface and strikes it, it is presumed to be lost through Auger neutralization. If it is directed away from the surface and towards the channeltron it is detected. By considering the distribution of initial Rydberg atom velocities and trajectories it is possible to calculate the fraction of incident atoms that will be detected as ions, and hence the normalized surface ion signal, for any chosen angle of incidence and applied collection field.

Figure 3 contains lines that show the trajectories of Rydberg atoms incident at $\theta = 10°$. The spacing of the pair of trajectories included in each figure corresponds to illumination of one full period of the electrode array. The positions at which the trajectories of atoms within this period intersect the locus of ionization points are highlighted in either white or black. Those atoms that ionize at locations shown in white are collected by the ion collection field and detected, whereas those that ionize in locations shown in black are lost to the surface. Clearly, as the ion collection field is increased, an increasing fraction of the product ions is collected and at an ion collection field of ~ 800 V cm^{-1} essentially all the incident Rydberg atoms are detected as ions. It should be noted that since the atoms are incident at near-grazing angles of incidence, θ, ionization preferentially occurs at points near the peaks in the ionization profile. This throws a "shadow" that limits the number of Rydberg atoms that ionize close to the surface thereby enhancing the overall ion collection efficiency. As the incidence angle, θ, is decreased, ionization becomes increasingly focused near the peaks in the ionization profile leading (at the smaller ion collection fields) to increases in the fraction of incident Rydberg atoms that are detected as ions.

The effect of the ion collection field on the (calculated) ion signal is illustrated in Fig. 4 for the same electrode geometry and angle of incidence as in Fig. 3 and several representative values of electrode bias. For each electrode bias considered, the normalized ion signal initially increases monotonically with ion collection field before reaching a plateau, i.e., the value 1.0, beyond which every incident Rydberg atom is detected as an ion. Interestingly, the ion signals predicted at the lower ion collection fields initially increase with increasing electrode bias but then saturate and become essentially independent of electrode bias. This results because, although incident atoms ionize at ever greater distances from the surface, the fraction of the product ions that is directed away from the surface remains little changed. The results of simulations for angles of incidence $\theta = 5°$ and $15°$ and the same electrode biases are

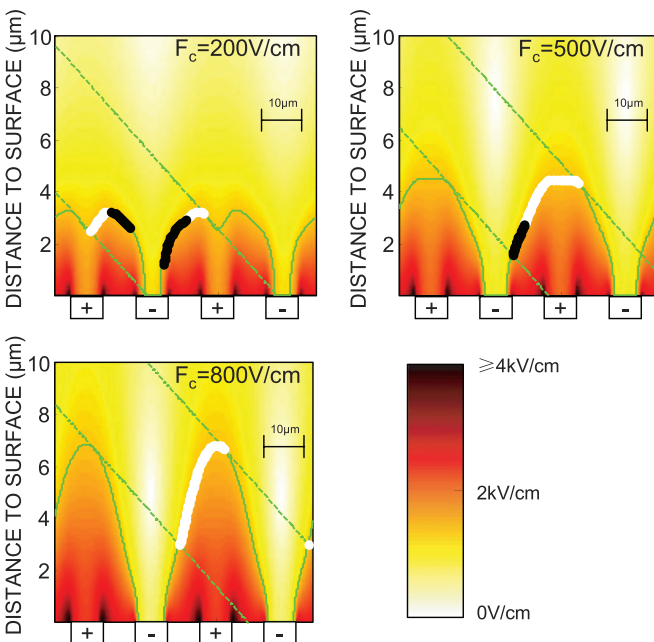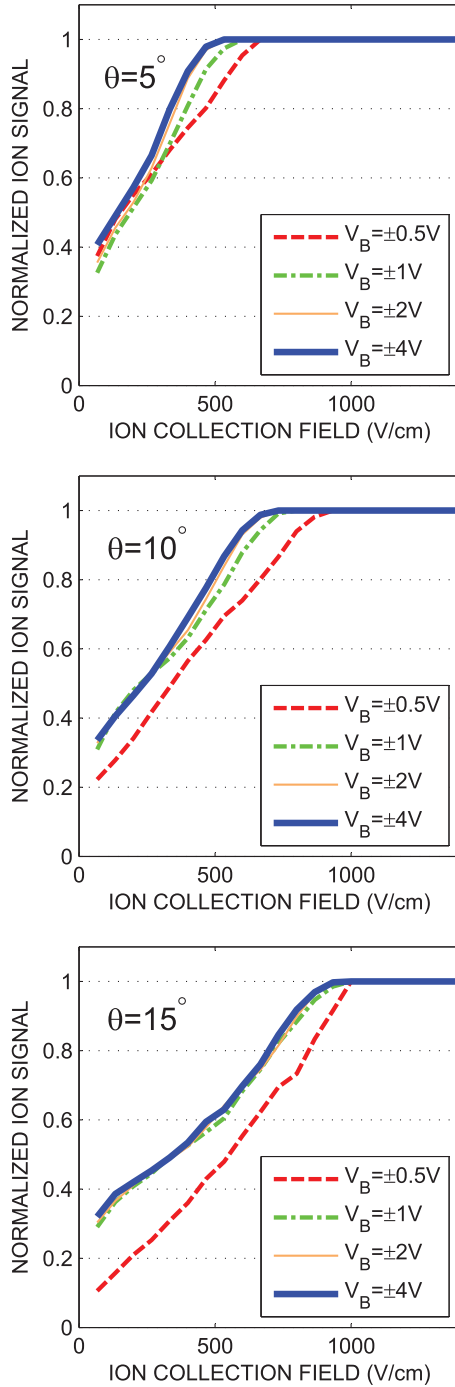FIG. 4. (Color online) Calculated normalized surface ion signals for $n = 23$ Rydberg atoms incident on an electrode array with widths and spacings of 8 μm for the angles of incidence and electrode biases V_B indicated.

IV. RESULTS AND DISCUSSION

Representative experimental results showing how the surface ion signals depend on ion collection field are presented in Fig. 5. The figure includes data for Rydberg atoms with $n = 18$, 23, and 32 recorded using an angle of incidence $\theta \sim 9°$ and an electrode array with widths and spacings of 8 μm. (The tuning range of the laser limited measurements to states with $n \geqslant 18$.) Tests revealed that the electrode biases used for each
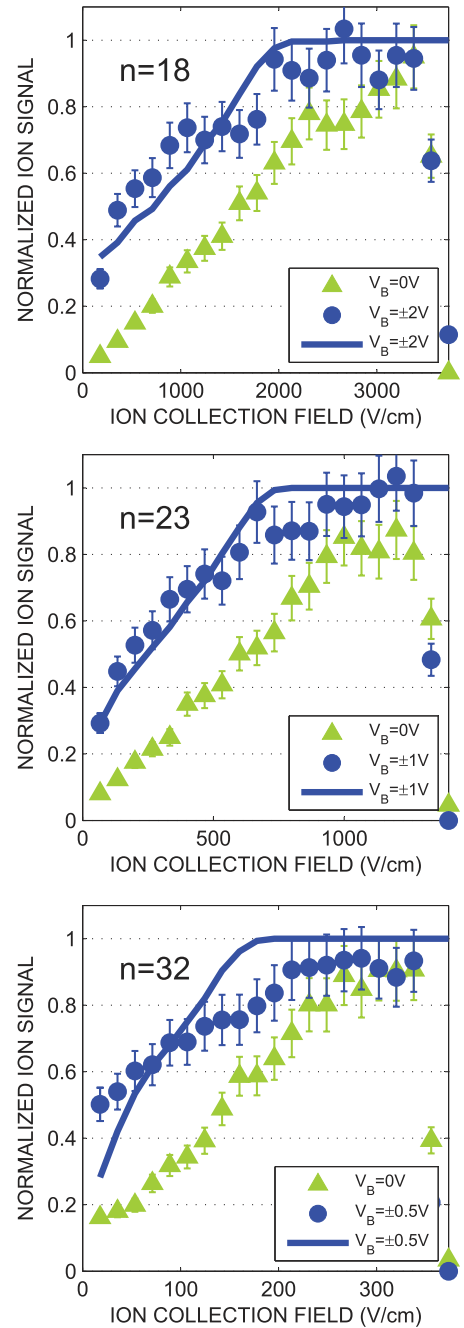

FIG. 5. (Color online) Measured (symbols) and calculated (lines) normalized surface ion signals as a function of ion collection field for atoms with the values of n indicated incident at $\theta \sim 9°$ on an electrode array with widths and spacings of 8 μm. The electrode biases V_B employed are also indicated.

also included in Fig. 4. While these display the same general characteristics as the results for $\theta = 10°$, it is evident that as the angle of incidence is decreased, the ion signals expected at the lower ion collection fields are increased and that the plateau where every incident Rydberg atom is detected as an ion is reached at smaller ion collection fields. For all angles of incidence, however, biases of $V_B \sim \pm 1$ V are sufficient to essentially saturate the detected ion signal.

value of n were sufficient to saturate the ion signals observed at the smaller values of applied field. The results in Fig. 5 thus represent the largest surface ion signals that can be achieved by biasing the electrodes.

The sharp cutoff in the ion signal evident at high ion collection fields results from direct field ionization of the incident Rydberg atoms by the collection field. Such ions are created relatively far from the surface immediately upon turn-on of the collection field and are discriminated against by the arrival time gating used to identify those ions produced in Rydberg atom-surface interactions. The threshold for such direct field ionization is consistent with that expected for adiabatic ionization, demonstrating that in fields that typically rise from 0 to 1 kV cm^{-1} in $\sim$1 μs, i.e., that have slew rates of $\sim$10^9 V cm^{-1} s^{-1}, the initial states evolve adiabatically. However, detailed measurements using $m = 1$ lithium Rydberg states with $n\sim$18 have shown that for such states the probability of adiabatic passage through avoided crossings can remain large even for slew rates of $\sim$1–2 $\times$ 10^{10} V cm^{-1} s^{-1} [29]. In the present work, the Rydberg atoms (which have velocities $\sim$4 $\times$ 10^2 m s^{-1}) encounter local fields that typically change by $\sim$1–2 kV cm^{-1} on length scales of $\sim$10 μm (see Fig. 3) resulting in slew rates of $\sim$4–8 $\times$ 10^{10} V cm^{-1} s^{-1}. While these are somewhat larger than the thresholds observed for diabatic behavior using lithium $m = 1$ states, the avoided crossings for lithium $m = 1$ states are much less pronounced than is the case for the present xenon $m = 0$ states because the perturbations induced by the xenon core ion are much larger (as evidenced by the large quantum defects for low-ℓ xenon Rydberg states) and because core interactions increase with decreasing $|m|$ [30]. In consequence, given the presence of much stronger avoided crossings, it is reasonable to expect that the incident xenon Rydberg atoms will evolve (predominantly) adiabatically as the surface is approached.

Each data set includes measurements taken with both sets of electrodes grounded, i.e., with no differential bias applied. The observed normalized ion signal increases steadily as the ion collection field is increased and its behavior mirrors that seen earlier at an oxidized Si(100) surface [22]. This similarity is attributed to the areas of exposed glass substrate between the electrodes. These areas are highly insulating and will be subject to similar surface charging as an oxidized Si(100) surface. While stray patch fields also exist above the electrode surfaces, those present above the insulating regions are larger and because of the "shadowing" effect discussed earlier will, in the absence of any applied electrode biases, tend to dominate ionization at the surface.

For each value of n application of the electrode bias leads to a marked increase in the observed ion signals that is particularly pronounced at the lower ion collection fields. Because of their larger physical size and weaker binding, higher-n atoms ionize in weaker fields and can therefore be efficiently detected using smaller electrode biases and ion collection fields. In each case, for sufficiently high electrode biases and ion collection fields, essentially all the incident Rydberg atoms, can be detected as ions. Figure 5 also includes the results of simulations. For $n = 18$ and 23, the simulations are in reasonable agreement with the experimental observations indicating that the measured ion signals can

indeed be attributed to field ionization of the incident Rydberg atoms in the combined field that results from biasing the electrode array and application of the ion collection field. For $n = 32$, the rise in the normalized ion signal is somewhat broader than suggested by the simulations. However, the biases applied, while sufficient to achieve saturation, are relatively low and stray surface patch fields might be sufficient to significantly perturb the calculated surface fields and account for at least some of the broadening.

The effects of electrode size are demonstrated in Fig. 6 which shows data for $n = 18$ Rydberg atoms incident at $\theta\sim$9$°$ on electrode arrays with widths (separations) of 4 μm (4 μm), 8 μm (8 μm), and 16 μm (16 μm). In each case the biases applied are sufficient to saturate the ion signals observed at the lower ion collection fields. This is illustrated by including data recorded at multiple bias voltages. While similar enhancements in the ion signals recorded at the lower ion collection fields can be achieved using all three electrode arrays, the electrode biases that must be applied to achieve this enhancement (and saturation of the ion signal) increase with electrode size. For the 4-μm electrode array maximal ion signals at the lower ion collection fields are achieved with biases above $\sim$$\pm$0.8 eV whereas for the 8- and 16-μm arrays biases above $\sim$$\pm$2 and $\sim$$\pm$3 V, respectively, are necessary. Figure 6 also includes the results of measurements using $n = 18$ atoms incident at $\theta\sim$5$°$ on the 8-μm electrode array. As predicted by the simulations (see Fig. 4), a decrease in the angle of incidence leads to an increase in the ion signal seen at the smaller ion collection fields.

As a further test of the present model, data were also recorded at an asymmetric electrode array comprising two sets of interleaved electrodes of different widths. Results using such an array having electrodes of widths 5 and 25 μm separated by 5 μm are shown in Fig. 7. A marked asymmetry in the observed ion signals is seen at low ion collection fields depending on which set of electrodes receives the (equal but opposite) positive and negative biases. In particular, at low ion collection fields, the measured ion signal is significantly larger when the positive bias is applied to the narrower set of electrodes. Such an asymmetry is predicted by the simulations and can be understood by reference to Figs. 7(b) and 7(c) which show the magnitude of the calculated fields near the surface for an ion collection field of 400 V cm^{-1} together with the locus of points at which ionization of $n = 23$ atoms will occur. Application of the positive bias in the 5-μm electrodes results in the production of strong local fields in their vicinity that have components directed away from the surface. Therefore, as illustrated in Fig. 7(b), those Rydberg atoms that ionize both above and near to these electrodes produce ions that are directed away from the surface and detected. Ions generated near the wider negatively biased electrodes are attracted to the surface and lost. In all, the calculations suggest that $\sim$71% of the incident Rydberg atoms will be detected as ions. The situation is reversed when a negative bias is applied to the 5-μm electrodes. Strong fields again appear above these electrodes but have components directed towards the surface. Ions produced above or near to these electrodes are thus now lost to the surface. Only those ions produced closest to the wider positively biased electrodes are collected and a smaller
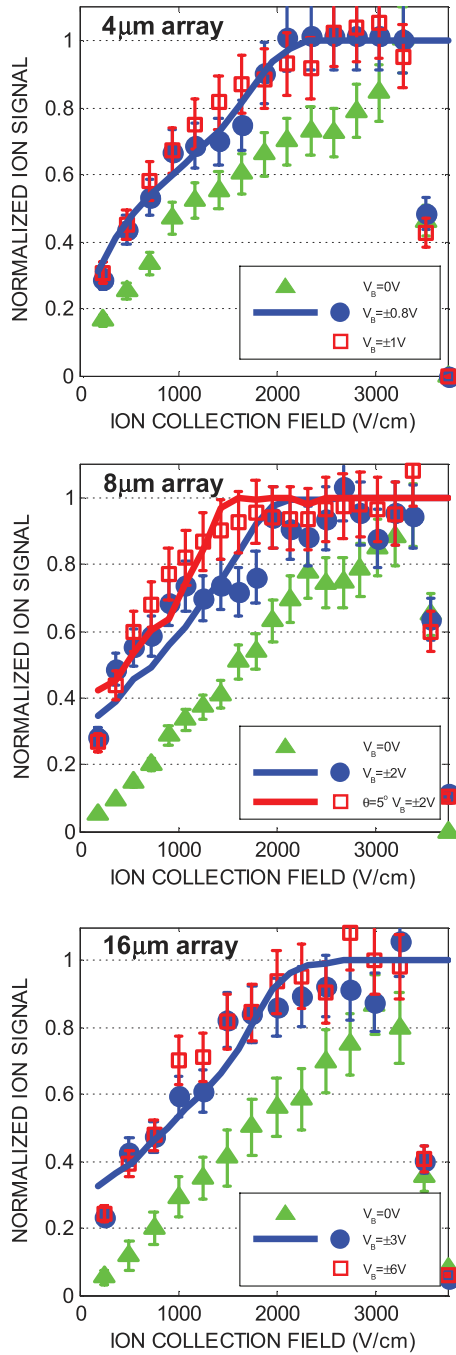
FIG. 6. (Color online) Measured (symbols) and calculated (lines) normalized surface ion signals as a function of ion collection field for $n = 18$ atoms incident at $\theta \sim 9°$ on electrode arrays with the widths and spacings and the biases V_B indicated. Measurements for $\theta \sim 5°$ are included with the results for the 8-μm array.
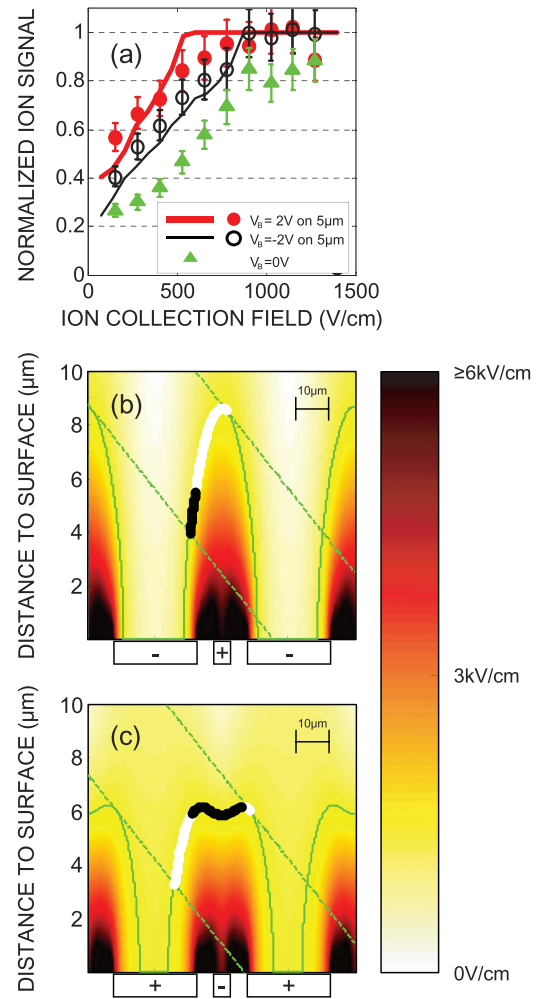

FIG. 7. (Color online) (a) Measured (symbols) and calculated (lines) normalized surface ion signals as a function of ion collection field for Rydberg atoms with $n = 23$ incident at $\theta \sim 9°$ on an asymmetric array having electrodes of widths of 5 and 25 μm separated by 5 μm. The bias voltage is ± 2 V and results are included with both the positive ($\bullet$) and negative ($\bigcirc$) bias applied to the 5-μm-wide electrodes. (b), (c) Calculated magnitude of the electric field above the electrodes with (b) the positive bias applied to the 5-μm electrode and (c) the 25-μm electrode, and an ion collection field of 400 V cm^{-1}. The dashed lines indicate trajectories of atoms incident at 9°. The solid lines show the locus of points where the field is sufficient to ionize $n = 23$ atoms. Atoms ionized at points indicated by white (black) dots are collected by the ion collection field (lost to the surface).

fraction, $\sim 57\%$, of the incident Rydberg atoms is detected as ions.

Because Laplace's equation has scale symmetry, the ion collection efficiencies expected for different values of n, different electrode sizes and biases, and different ion collection fields possess interesting scaling properties. Given that the expansion coefficients A_i in Eq. (6) scale as the bias voltages $\pm V_B$, the magnitude of the total electric field at a point in the presence of an ion collection field F can be written in terms of the dimensionless variables x/D, z/D, and $FD/2\pi V_B$ as

$$|E(x,z,F)| = \frac{2\pi V_B}{D} \left[\left(\sum_{i=1}^{N} a_i i \, \sin \frac{2\pi i}{D} x \, e^{-\frac{2\pi i}{D} z} \right)^2 \right.$$
$$\left. + \left(\frac{FD}{2\pi V_B} + \sum_{i=1}^{N} a_i i \, \cos \frac{2\pi i}{D} x \, e^{-\frac{2\pi i}{D} z} \right)^2 \right]^{1/2},$$
(8)

where $a_i = A_i / V_B$, i.e.,

$$|E(x,z,F)| = \frac{2\pi V_B}{D} f\left(\frac{x}{D}, \frac{z}{D}, \frac{FD}{2\pi V_B}\right). \tag{9}$$

To field ionize atoms with principal quantum number n we require

$$\frac{2\pi V_B}{D} f\left(\frac{x}{D}, \frac{z}{D}, \frac{FD}{2\pi V_B}\right) = \frac{1}{16n^4}. \tag{10}$$

Similarly, to ionize atoms with principal quantum number n' using electrodes with period D', biases of $\pm V_B'$, and an ion collection field F' requires

$$\frac{2\pi V_B'}{D'} f\left(\frac{x}{D'}, \frac{z}{D'}, \frac{F'D'}{2\pi V_B'}\right) = \frac{1}{16n'^4}. \tag{11}$$

If the electrode widths and biases are scaled as

$$D' = D\frac{n'^2}{n^2}, \quad V_B' = V_B\frac{n^2}{n'^2}, \tag{12}$$

and the field as

$$F' = F\frac{n^4}{n'^4}, \tag{13}$$

Eq. (11) yields

$$\frac{2\pi V_B}{D} f\left(\frac{\frac{n^2}{n'^2}x}{D}, \frac{\frac{n^2}{n'^2}z}{D}, \frac{FD}{2\pi V_B}\right) = \frac{1}{16n^4}, \tag{14}$$

i.e., the locations at which ionization occurs scale as n'^2/n^2. The results of this are illustrated in Fig. 8 which shows calculated normalized ion signals plotted as a function of scaled ion collection field, $E_O = E/E_T(n)$, where $E_T(n)$ is the threshold ionization field, $1/16n^4$ a.u., for several values of n. The electrode dimensions and biases used in the simulations are listed in the inset and are scaled as in Eq. (12). (The particular biases employed were chosen to optimize the
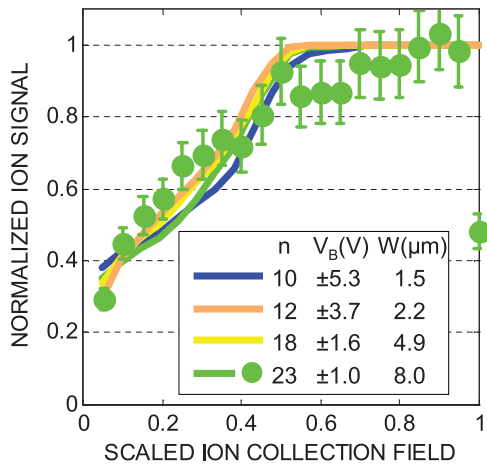

FIG. 8. (Color online) Calculated normalized surface ion signals plotted as a function of scaled ion collection field $E_O = E_C/E_T(n)$, where $E_T(n)$ is the threshold field for field ionization, for Rydberg atoms incident at $\theta \sim 9°$. The values of n, electrode widths and spacings W, and biases $\pm V_B$ considered are as indicated (see text). The symbols show experimental data recorded for $n = 23$ atoms.
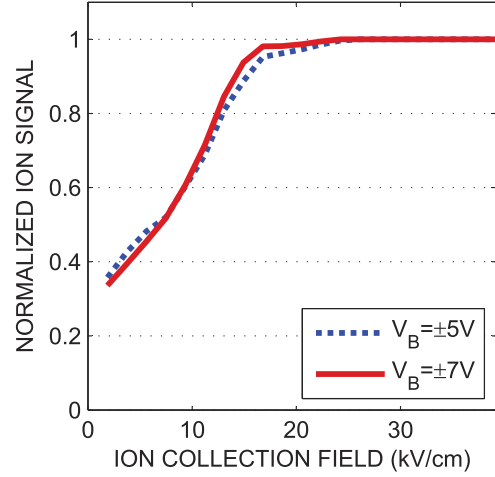

FIG. 9. (Color online) Calculated normalized surface ion signals as a function of ion collection field for $n = 10$ Rydberg atoms incident at $\theta = 5°$ on an electrode array with widths and spacings of 1.5 μm and the biases V_B indicated.

ion signals at the lower ion collection fields, i.e., at E_O values of ~ 0.25.) As expected, the various simulation results display very similar characteristics. In each case, greater than $\sim 50\%$ of the incident Rydberg atoms are detected as ions for scaled ion collection fields $E_O \sim 0.25$, and this increases to near 100% for $E_O \sim 0.5$.

The fact that a sizable fraction of the incident Rydberg atoms can be detected even using fields that are only 25% of that required to induce direct field ionization suggests that surface ionization might form a convenient technique with which to detect Rydberg atoms, especially low-n Rydberg atoms for which the threshold fields for ionization are large, $\sim 38 \, \text{kV cm}^{-1}$ at $n = 10$, and require careful electrode design to prevent electrical breakdown. Breakdown is suppressed when using micrometer-scale electrode arrays because the potential differences required to generate very strong local fields are small. Any spurious charged particles that might be produced do not gain sufficient energy from the field before striking an electrode to sustain a discharge either through ionization of background gas or through secondary emission from the electrode surfaces. As demonstrated by the simulations in Fig. 9, for $n = 10$ the use of 1.5-μm electrodes and biases of ± 5 V should, for an angle of incidence of 5°, allow detection of $\sim 60\%$ of the incident atoms using a 10 kV cm^{-1} ion collection field. Greater than $\sim 40\%$ should still be detected using an ion collection field of only ~ 5 kV cm^{-1}. However, since ionization might occur at atom-surface separations as small as ~ 300 nm, finite electrode thickness might become a concern.

V. SUMMARY

The present work demonstrates that Rydberg atom-surface interactions can be controlled using biased micrometer-scale electrode arrays. In particular, application of even small biases can result in field ionization well above the target surface allowing the resulting product ions to be detected using relatively modest ion collection fields and pointing to the

application of surface ionization in the detection of low-n Rydberg atoms. The data further illustrate the critical role that local surface fields can play in determining the nature of atom-surface interactions.

[1] J. M. Obrecht, R. J. Wild, and E. A. Cornell, Phys. Rev. A **75**, 062903 (2007).

[2] J. Labaziewicz, Y. Ge, D. R. Leibrandt, S. X. Wang, R. Shewmon, and I. L. Chuang, Phys. Rev. Lett. **101**, 180602 (2008).

[3] A. Gaëtan, Y. Miroshnychenko, T. Wilk, A. Chotia, M. Viteau, D. Comparat, P. Pillet, A. Browaeys, and P. Grangier, Nat. Phys. **5**, 115 (2009).

[4] L. Isenhower, E. Urban, X. L. Zhang, A. T. Gill, T. Henage, T. A. Johnson, T. G. Walker, and M. Saffman, Phys. Rev. Lett. **104**, 010503 (2010).

[5] J. D. Carter, O. Cherry, and J. D. D. Martin, Phys. Rev. A **86**, 053401 (2012).

[6] A. Safavi-Naini, P. Rabl, P. F. Weck, and H. R. Sadeghpour, Phys. Rev. A **84**, 023412 (2011).

[7] D. A. Hite, Y. Colombe, A. C. Wilson, K. R. Brown, U. Warring, R. Jördens, J. D. Jost, K. S. McKay, D. P. Pappas, D. Leibfried, and D. J. Wineland, Phys. Rev. Lett. **109**, 103001 (2012).

[8] C. I. Sukenik, M. G. Boshier, D. Cho, V. Sandoghdar, and E. A. Hinds, Phys. Rev. Lett. **70**, 560 (1993).

[9] J. A. Crosse, S. Å. Ellingsen, K. Clements, S. Y. Buhmann, and S. Scheel, Phys. Rev. A **82**, 010901(R) (2010).

[10] B. C. Stipe, H. J. Mamin, T. D. Stowe, T. W. Kenny, and D. Rugar, Phys. Rev. Lett. **87**, 096801 (2001).

[11] S. Kuehn, R. F. Loring, and J. A. Marohn, Phys. Rev. Lett. **96**, 156103 (2006).

[12] A. Tauschinsky, R. M. T. Thijssen, S. Whitlock, H. B. van Linden van den Heuvell, and R. J. C. Spreeuw, Phys. Rev. A **81**, 063411 (2010).

[13] J. D. Carter and J. D. D. Martin, Phys. Rev. A **83**, 032902 (2011).

[14] H. Hattermann, M. Mack, F. Karlewski, F. Jessen, D. Cano, and J. Fortágh, Phys. Rev. A **86**, 022511 (2012).

[15] P. Nordlander and F. B. Dunning, Nucl. Instrum. Methods Phys. Res., Sect. B **125**, 300 (1997).

[16] C. Oubré, P. Nordlander, and F. B. Dunning, J. Phys. Chem. B **106**, 8338 (2002).

[17] J. Sjakste, A. G. Borisov, and J. P. Gauyacq, Phys. Rev. A **73**, 042903 (2006).

[18] E. So, M. T. Bell, and T. P. Softley, Phys. Rev. A **79**, 012901 (2009).

[19] D. Wang, K. Huang, and S. Lin, Eur. Phys. J. D **54**, 699 (2009).

[20] N. N. Nedeljkovic and D. K. Bozanic, Phys. Rev. A **81**, 032902 (2010).

[21] S. B. Hill, C. B. Haich, Z. Zhou, P. Nordlander, and F. B. Dunning, Phys. Rev. Lett. **85**, 5444 (2000).

[22] D. D. Neufeld, H. R. Dunham, S. Wethekam, J. C. Lancaster, and F. B. Dunning, Phys. Rev. B **78**, 115423 (2008).

[23] Y. Pu, D. D. Neufeld, and F. B. Dunning, Phys. Rev. A **81**, 042904 (2010).

[24] D. D. Neufeld, Y. Pu, and F. B. Dunning, Nucl. Instrum. Meth. Phys. Res. B **269**, 1288 (2011).

[25] E. So, M. Dethlefsen, M. Ford, and T. P. Softley, Phys. Rev. Lett. **107**, 093201 (2011).

[26] F. B. Dunning, S. Wethekam, H. R. Dunham, and J. C. Lancaster, Nucl. Instrum. Methods Phys. Res., Sect. B **258**, 61 (2007).

[27] D. D. Neufeld, H. R. Dunham, S. Wethekam, J. C. Lancaster, and F. B. Dunning, Surf. Sci. **602**, 1306 (2008).

[28] FineLine Imaging, 4733 Centennial Blvd., Colorado Springs, CO 80919, http://www.fineline-imaging.com.

[29] J. R. Rubbmark, M. M. Kash, M. G. Littman, and D. Kleppner, Phys. Rev. A **23**, 3107 (1981).

[30] M. L. Zimmerman, M. G. Littman, M. M. Kash, and D. Kleppner, Phys. Rev. A **20**, 2251 (1979).